



This is a repository copy of *Initial feasibility and challenges of hyperpolarized ^{129}Xe MRI in neonates with bronchopulmonary dysplasia.*

White Rose Research Online URL for this paper:

<https://eprints.whiterose.ac.uk/202181/>

Version: Published Version

Article:

Stewart, N.J. orcid.org/0000-0001-8358-394X, Higano, N.S. orcid.org/0000-0002-6233-161X, Mukthapuram, S. et al. (9 more authors) (2023) Initial feasibility and challenges of hyperpolarized ^{129}Xe MRI in neonates with bronchopulmonary dysplasia. *Magnetic Resonance in Medicine*, 90 (6). pp. 2420-2431. ISSN 0740-3194

<https://doi.org/10.1002/mrm.29808>

Reuse

This article is distributed under the terms of the Creative Commons Attribution-NonCommercial-NoDerivs (CC BY-NC-ND) licence. This licence only allows you to download this work and share it with others as long as you credit the authors, but you can't change the article in any way or use it commercially. More information and the full terms of the licence here: <https://creativecommons.org/licenses/>

Takedown



If you consider content in White Rose Research Online to be in breach of UK law, please notify us by emailing eprints@whiterose.ac.uk including the URL of the record and the reason for the withdrawal request.



eprints@whiterose.ac.uk
<https://eprints.whiterose.ac.uk/>

RAPID COMMUNICATION

Initial feasibility and challenges of hyperpolarized ^{129}Xe MRI in neonates with bronchopulmonary dysplasia

Neil J. Stewart^{1,2}  | Nara S. Higano^{1,3,4}  | Shanmukha Mukthapuram^{3,5} |

Matthew M. Willmering¹  | Wolfgang Loew⁴ | Michael West¹ |

Anita Arnsperger⁶ | Ronald Pratt⁴ | Madhwesha R. Rao² | Rolf F. Schulte⁷ |

Jim M. Wild²  | Jason C. Woods^{1,3,4} 

¹Center for Pulmonary Imaging Research, Pulmonary Medicine and Radiology, Cincinnati Children's Hospital Medical Center, Cincinnati, Ohio, USA

²POLARIS, Imaging Sciences, Department of Infection, Immunity & Cardiovascular Disease, University of Sheffield, Sheffield, UK

³Department of Pediatrics, University of Cincinnati College of Medicine, Cincinnati, Ohio, USA

⁴Department of Radiology, Cincinnati Children's Hospital Medical Center, Cincinnati, Ohio, USA

⁵The Perinatal Institute, Section of Neonatology, Perinatal and Pulmonary Biology, Cincinnati Children's Hospital Medical Center, Cincinnati, Ohio, USA

⁶Division of Respiratory Care, Cincinnati Children's Hospital Medical Center, Cincinnati, Ohio, USA

⁷GE Healthcare, Munich, Germany

Correspondence

Jason C. Woods, Center for Pulmonary Imaging Research, Cincinnati Children's Hospital Medical Center, 3333 Burnet Avenue, Cincinnati, OH 45229-3026, USA. Email: jason.woods@cchmc.org

Funding information

European Commission, Grant/Award Number: 713406; European Respiratory Society (ERS); NIH, Grant/Award Number: R01 HL146689; Thrasher Research Fund; Cincinnati Children's Research Foundation; the Parker B. Francis Fellowship

Abstract

Purpose: The underlying functional and microstructural lung disease in neonates who are born preterm (bronchopulmonary dysplasia, BPD) remains poorly characterized. Moreover, there is a lack of suitable techniques to reliably assess lung function in this population. Here, we report our preliminary experience with hyperpolarized ^{129}Xe MRI in neonates with BPD.

Methods: Neonatal intensive care patients with established BPD were recruited ($N = 9$) and imaged at a corrected gestational age of median:40.7 (range:37.1, 44.4) wk using a 1.5T neonatal scanner. 2D ^{129}Xe ventilation and diffusion-weighted images and dissolved phase spectroscopy were acquired, alongside ^1H 3D radial UTE. ^{129}Xe images were acquired during a series of short apneic breath-holds (~ 3 s). ^1H UTE images were acquired during tidal breathing. Ventilation defects were manually identified and qualitatively compared to lung structures on UTE. ADCs were calculated on a voxel-wise basis. The signal ratio of the ^{129}Xe red blood cell (RBC) and tissue membrane (M) resonances from spectroscopy was determined.

Results: Spiral-based ^{129}Xe ventilation imaging showed good image quality and sufficient sensitivity to detect mild ventilation abnormalities in patients with BPD. ^{129}Xe ADC values were elevated above that expected given healthy data in older children and adults (median:0.046 [range:0.041, 0.064] cm^2s^{-1}); the highest value obtained from an extremely pre-term patient. ^{129}Xe spectroscopy revealed a low RBC/M ratio (0.14 [0.06, 0.21]).

Conclusion: We have demonstrated initial feasibility of ^{129}Xe lung MRI in neonates. With further data, the technique may help guide management of infant lung diseases in the neonatal period and beyond.

KEYWORDS

bronchopulmonary dysplasia, hyperpolarized ^{129}Xe , lung MRI, neonatal MRI

Neil J. Stewart and Nara S. Higano contributed equally to this work.

This is an open access article under the terms of the [Creative Commons Attribution-NonCommercial-NoDerivs](https://creativecommons.org/licenses/by-nc-nd/4.0/) License, which permits use and distribution in any medium, provided the original work is properly cited, the use is non-commercial and no modifications or adaptations are made.

© 2023 The Authors. *Magnetic Resonance in Medicine* published by Wiley Periodicals LLC on behalf of International Society for Magnetic Resonance in Medicine.

1 | INTRODUCTION

Bronchopulmonary dysplasia (BPD) is a chronic lung disease of prematurity and major cause of short- and long-term morbidity and mortality in preterm infants.¹ Clinical understanding, prognostication, and individualized clinical care of infants with BPD remain modest. Moreover, evidence indicates that BPD in early life yields reduced cardiopulmonary function in childhood and beyond.^{2,3} Therefore, the ability to detect pulmonary dysfunction and quantify severity and phenotype in infancy would inform patient management strategies and improve short- and long-term respiratory outcomes. However, there are effectively no sensitive techniques to assess pulmonary functional deficits and microstructural abnormalities at an early age. Pulmonary function testing poses technical challenges and increased risks in infants (including sedation and thoracic compression⁴), and imaging modalities such as CT do not generally measure pulmonary function, and are used sparingly due to concerns over ionizing radiation exposure.⁵

Free-breathing 3D radial ¹H UTE MRI is a safe, non-ionizing alternative to CT for visualizing structural lung disease in neonates with BPD,^{6,7} and UTE-derived disease severity scoring has been shown to correlate with short-term respiratory outcomes.⁸ However, UTE MRI has thus far provided limited information on infant lung function. Preliminary data on the feasibility of free-breathing phase-resolved functional lung (PREFUL) ¹H imaging to assess ventilation and perfusion function have been reported in healthy neonates⁹ and in a cohort of infants with BPD,¹⁰ although further data are required to assess sensitivity. MRI of inhaled hyperpolarized (HP) ¹²⁹Xe gas is a safe, sensitive technique able to measure lung ventilation, microstructure, and gas exchange, and has been used extensively to assess adult and pediatric lung disease.^{11–14} In addition, diffusion-weighted MRI of both inhaled HP ³He^{15,16} and ¹²⁹Xe¹⁷ MRI can detect long-term lung functional changes in children born preterm with BPD imaged at school age. Altes et al. published a proof-of-concept study on preliminary findings of lung ventilation MRI in children from a few months to a few years old with a range of conditions, using HP ³He gas.¹⁸ However, the field has now largely transitioned to ¹²⁹Xe due to the scarcity of ³He, and HP ¹²⁹Xe gas MRI in infants has yet to be reported. Moreover, in-vivo acquisition of lung microstructural and gas exchange information with HP gas MRI has not been explored in infants using either ³He or ¹²⁹Xe.

Here, we report our initial experience in performing HP ¹²⁹Xe gas MRI in a small cohort of neonates with BPD. In addition to exploring the feasibility of ¹²⁹Xe ventilation MR imaging with 2D spiral-based pulse sequences,

we obtain preliminary data on lung microstructure and gas exchange with spiral-based diffusion-weighted and spectroscopic pulse sequences, respectively.

2 | METHODS

2.1 | Study cohort

Subjects were recruited from the neonatal intensive care unit (NICU) at Cincinnati Children's Hospital Medical Center with Institutional Review Board approval and informed parental consent. Inclusion criteria were as follows: inpatient status in the NICU with established lung disease; chronological age of 0–6 mo old; clinical stability to tolerate MRI; ability to maintain SpO₂ > 88% on clinically indicated respiratory support; and body size compatible with a neonatal-sized MRI scanner (≤4.5 kg). Further, subjects were on various levels of respiratory support, with no change for the 24 h preceding MRI. Respiratory support levels were as follows: (1) no use of respiratory support (i.e., breathing room air); (2) use of oxygen with nasal cannula (NC) at ≤2 L/min; and (3) use of high flow nasal cannula (HFNC) at ≥2 L/min, continuous positive airway pressure (CPAP), or nasal non-invasive ventilation using a RAM Cannula interface (Neotech, Valencia, CA), with FiO₂ < 50%. None of the patients in this study were on invasive support. Respiratory support for each patient is summarized in Table 1, along with disease severity graded according to the criteria defined in Jensen et al.¹⁹; six patients had grade 1 BPD, two had grade 2 BPD, and one had “no BPD” at the time of MRI.

Exclusion criteria were as follows: use of general anesthesia within 24 h or other sedation within 4 h prior to MRI; use of extracorporeal membrane oxygenation (ECMO) support; evidence of any respiratory infection within 1 wk of MRI; significant or suspected genetic abnormality, chromosomal abnormality, neurologic disorder, or muscular dystrophy that may affect lung development; congenital heart disease; uncontrolled atrial or ventricular arrhythmia; open surgical wounds; need for inotropic support; need for pulmonary vasodilator agents; and standard MRI exclusion criteria.

In this preliminary feasibility study, 10 subjects (5F, 5M) were recruited. One subject (#5) was discharged from the NICU prior to MRI. Subject demographics are shown in Table 1. All subjects who underwent imaging had a clinical diagnosis of BPD, with a corrected gestational age (GA) at birth of median (range) 26.9 (22.3, 31.6) wk and age at MRI of 40.7 (37.1, 44.4) wk.

Subjects were imaged while on their clinically indicated settings for respiratory support, except during each ~3 s ¹²⁹Xe breath-hold, for which clinical oxygen flow

TABLE 1 Subject demographic and clinical details

ID	Sex	BPD severity grade ^b	GA at birth (wk)	Weight at birth (kg)	GA at MRI (wk)	Weight at MRI (kg)	Respiratory support at MRI
1	F	Grade 1	28.6	1.11	39.3	2.945	NC, 0.25 L/min, 100% FiO ₂
2	M	Grade 2	26.0	1.00	38.0	1.830	HFNC, 3 L/min, 40% FiO ₂
3	M	Grade 3	24.0	0.51	40.7	3.09	NC, 1 L/min, 30% FiO ₂
4	M	Grade 2	22.3	0.46	43.0	3.66	NC, 0.5 L/min, 100% FiO ₂
5	F	N/A: RDS	28.1	0.75	N/A	N/A	N/A
6	F	Grade 1	25.1	0.57	41.3	2.480	NC, 0.5 L/min 100% FiO ₂
7	M	Grade 2	27.3	0.56	44.4	3.930	NC, 2 L/min, 23% FiO ₂
8	F	Grade 3	26.9	0.78	38.1	2.350	HFNC, 4 L/min, 28% FiO ₂
9	F	Grade 1	26.9	0.78	41.1	3.890	None
10	M	Grade 2	31.6	1.99	37.1	3.040	HFNC, 2 L/min, 23% FiO ₂
Total ^a	4F/5 M	1 none 3 Grade 1 4 Grade 2 2 Grade 3	26.9 (22.3, 31.6)	0.78 (0.46, 1.99)	40.7 (37.1, 44.4)	3.04 (1.83, 3.93)	1 none 5 NC 3 HFNC

Abbreviations: GA, gestational age (GA at MRI is “corrected GA”); HFNC, high-flow nasal cannula; NC, nasal cannula; RDS, respiratory distress syndrome.

^aData for totals exclude Subject 5, who was discharged prior to MRI. Data are reported as median (range), where relevant.

^bGrade is defined according to the criteria outlined by Jensen et al.¹⁷

was temporarily paused. Intravenous contrast agents and sedation/anesthesia were not administered for imaging. Subjects were fed, swaddled, and equipped with ear protection prior to imaging.

2.2 | MRI methods

MRI was performed on a multi-nuclear 1.5T neonatal-sized MRI system^{20,21} (originally an orthopedic scanner from ONI Medical Systems; currently GE Healthcare HDx) (Figure 1A). A home-built ¹²⁹Xe/¹H switched-frequency high-pass birdcage coil (Figure 1B) was used to image both nuclei rapidly without altering the subject’s position.^{22,23} In between ¹H and ¹²⁹Xe scans, the transmit/receive frequency of the coil was switched by adding/removing capacitor banks via pushing/pulling of mechanical rods on the coil and switching the BNC cables from one TR switch to the other. This was done while the subject was in the scanner bore and took between 30 s and 1 min.

Table 2 provides a summary of the acquisitions that were performed in each subject. ¹²⁹Xe images of lung ventilation were acquired using 2D slice-selective spoiled gradient echo sequences; initial $N=2$ subjects with a sequential Cartesian readout (FOV = 24 cm, resolution = 3.75 × 3.75 × 9.0 mm³, flip angle [FA] = 11°,

scan time per slice ~0.5 s), and the remaining $N=7$ subjects with a spiral readout (FOV = 24 cm, resolution = 3 × 3 × 7.5 mm³, 12 spiral arms, 80 read-out points per arm, read-out bandwidth = 62.5 kHz, FA = 20°, TR = 18.9 ms, scan time per slice ~0.2 s).

¹²⁹Xe diffusion-weighted images were acquired using a 2D diffusion-weighted sequence with a spiral readout (similar Reference 24), with two b-values (0 and 5 s.cm⁻²) and a diffusion time $\Delta=3$ ms (diffusion gradient ramp time $\tau=0.28$ ms; no gap between bi-polar elements, i.e., $\Delta=\delta$). These parameters were selected to be in between published values from previous work in small animals²⁵ and adults²⁶ with ¹²⁹Xe gas, and also guided by previous ex-vivo infant lung MRI work with ³He gas.²⁷ Other parameters were: FOV = 24 cm, resolution = 3.75 × 3.75 × 7.5 mm³, 10 spiral arms per diffusion interleave, read-out bandwidth = 62.5 kHz, FA = 15.5°, TR = 22.9 ms, scan time per slice ~0.45 s.

Dynamic MR spectra of dissolved-phase ¹²⁹Xe were acquired (see Reference 28) with; spectral bandwidth = 31.25 kHz, resolution = 61 Hz per point, FA = 20° using a frequency-selective RF pulse designed using an iterative method (pulse width = 1 ms, bandwidth = 800 Hz),²⁹ TR = 25.7 ms.

In $N=1$ subject, an exploratory 2D dynamic radial projection ventilation image acquisition was performed (see References 30,31) with FOV = 18 cm, in-plane

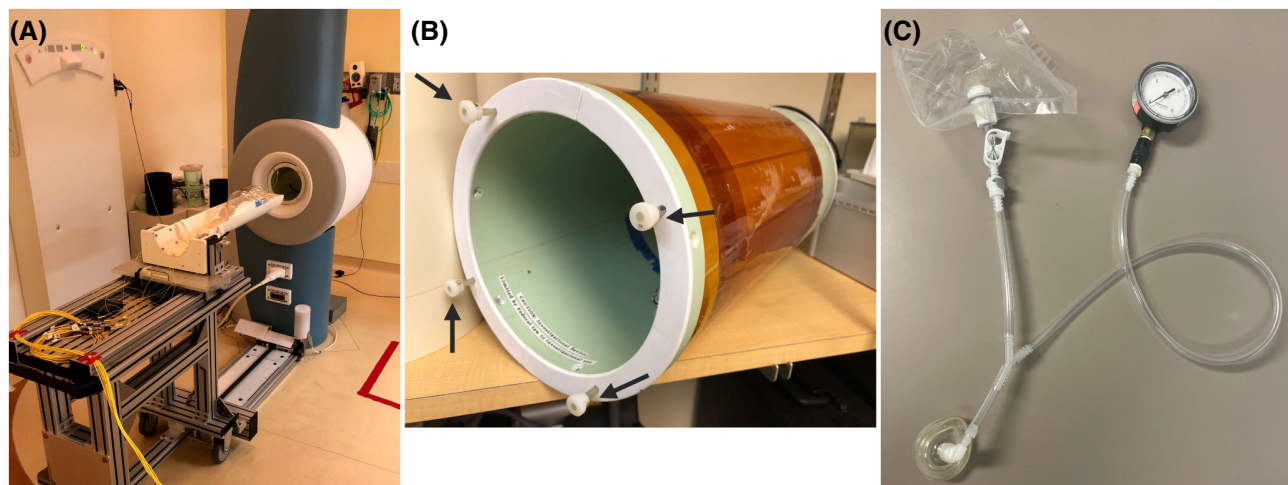


FIGURE 1 MRI equipment set-up: (A) neonatal MRI scanner and patient table. (B) ^1H - ^{129}Xe RF coil, with frequency switching via insertion/withdrawal of mechanical rods (arrows). (C) Breath-hold gas delivery apparatus with Tedlar bag, pressure gauge, and clinically available neonatal face mask.

TABLE 2 Subject scan success rates and quantitative metrics

Patient ID	Ventilation			Diffusion			Dissolved phase	
	Cartesian	Spiral	Radial	Spiral		Spectroscopy		
ID	Acquired?	Acquired?	No. of defects (struct ^b)	Acquired?	Acquired?	ADC _{mean} (cm ² s ⁻¹)	Acquired?	RBC:M ratio
1	Yes, unusable	No	-	No	No	-	No	-
2	Yes, unusable	No	-	No	No	-	No	-
3	No	Yes	2 (0)	No	No	-	Yes	0 ^a
4	No	Yes	8 (6)	No	Yes	0.064 ± 0.033	Yes	0.06
6	No	Yes, unusable	-	No	Yes, unusable	-	Yes	0 ^a
7	No	Yes	6 (4)	No	Yes	0.044 ± 0.021	Yes	0.21
8	No	Yes	5 (4)	No	Yes	0.041 ± 0.026	Yes	0.08
9	No	Yes	7 (5)	No	Yes	0.048 ± 0.027	Yes	0.16
10	No	Yes	1 (1)	Yes	Yes, unusable	-	Yes	0.19
No. (%) Successful overall	0/9 (0%)	6/9 (67%)	-	1/9 (11%)	4/9 (44%)	-	7/9 (78%)	-
No. (%) Successful of attempted	0/2 (0%)	6/7 (86%)	-	1/1 (100%)	4/6 (67%)	-	7/7 (100%)	-
Median (range)	-	-	5.5 (1, 8)	-	-	0.046 (0.041, 0.064)	-	0.08 (0, 0.21)

^a RBC peak too small for fitting.

^b Number of defects that appear to correspond to underlying structural defects on ^1H MRI.

resolution = $1.88 \times 1.88 \text{ mm}^2$, 2000 spokes with golden angle ordering, bandwidth = 62.5 kHz, FA = 3°, TR = 11.1 ms.

Isotopically-enriched ^{129}Xe was polarized to ~40% using a commercial polarizer (Model 9820; Polarean Inc., Durham, NC, USA). Doses of ^{129}Xe were delivered using

a clinically available neonatal facemask via Tedlar bag compression not exceeding 15 cm H₂O by hand by a neonatologist (see Figure 1C). Breath-hold apnea of ~3 s in duration was induced, with any clinically-indicated oxygen flow temporarily paused for the duration of the breath-hold. Data were acquired repeatedly before, during,

and after the breath-hold (total period of ≥ 10 s) to obtain several time series of data. (Quantitative analysis was only performed on a single set of such dynamic images acquired during breath-hold.)

3D radial ^1H UTE structural images were acquired during tidal breathing (FOV = 18 cm, resolution = 0.7 mm^3 , FA = 5° , TR = 5.0 ms, TE = ~ 0.2 ms, bandwidth = 250 kHz, 200 k projections, duration = ~ 16 min); see for example References 6–8,32. The total scan duration (^1H + ^{129}Xe components) was between 30 and 45 min.

2.3 | Image processing and analysis

Spiral ventilation images were gridded,³³ (Hanning) filtered, and Fourier transformed. Ventilation defects were manually identified and counted slice-by-slice on the first dynamic phase that displayed adequate SNR for all slices. A single dynamic image series was chosen for analysis and presentation rather than the average image, as this was assumed to be more sensitive to subtle and temporally-variant defects. SNR was calculated in the central slice using a signal region of interest in the bottom of the left lung.

Diffusion-weighted spiral images were reconstructed separately for each b-value by the same gridding algorithm. The $b = 0$ images were manually segmented to create a mask of lung signal, and the ADC was calculated pixel-wise using a mono-exponential fit of the relative signal intensities of the images from the two diffusion interleaves.

Dissolved-phase ^{129}Xe spectral data were processed as follows. The first second of data was discarded, and the remaining free induction decays were phased and denoised using Tucker decomposition.³⁴ Spectra acquired between 1 and 2 s after starting the acquisition were averaged, and dissolved phase and gas phase peaks were fitted separately using double Lorentzian and single Lorentzian functions, respectively (see e.g., Reference 35) to derive relative signal amplitudes. Due to the small RBC resonance (see the Results section), the SNR of this resonance was insufficient to fit individual spectra to quantify cardiogenic oscillations.^{28,36}

2.4 | Safety monitoring

Heart rates and oxygen saturation levels were monitored prior to, immediately following, and at 2 min after each ^{129}Xe breath-hold. Provided that the subject's heart rate and SpO_2 returned to within 40 beats/min and 8% of their baseline values, respectively, the examination was continued. Clinical records were reviewed at Day 1 and

Day 10 following MRI (Day 0) for signs of sedation. The N-PASS (Neonatal Pain, Agitation, and Sedation Scale) system was used.³⁷ This is currently the only tool for assessing the level of sedation in critically ill infants and is performed routinely on every inpatient in our NICU. The sedation score ranges from 0 through -10 : a score of 0 indicates no sedation; a score of -2 through -5 indicates light sedation; and a score of -5 through -10 indicates deep sedation. An adverse event was defined as a decrease in the sedation score by more than three points between baseline and follow-up or a score lower than -3 at follow-up, with no relation to ongoing clinical management.

3 | RESULTS

There were no adverse events for any subjects during or after imaging, and no examinations were ended prematurely. All heart-rate and SpO_2 values stayed within defined limits at 2 min after each inhalation. Mild and transient O_2 desaturations were observed immediately after administration, with a mean decrease in SpO_2 of $-4.5 \pm 4.8\%$ over all patients (all doses, see Table S1), which recovered to pre-dose values within 10–20 s. All patients received an N-PASS sedation score of 0 (no sedation) at all follow-up time-points.

Image quality obtained from Cartesian spoiled gradient echo acquisitions was poor in the initial two subjects, with inconsistent signal appearance across slices (see the Discussion section). Thus, 2D spiral acquisitions were used for ^{129}Xe lung ventilation imaging in all subsequent patients (see Methods). Qualitatively, spiral acquisitions showed moderate to good image quality across several temporal phases. An example of the images acquired during the first five phases, and the average of such images, is shown in Figure S1. Figure 2 shows example images from a single dynamic phase (the one that was chosen for analysis) acquired in four different subjects. The SNR (calculated in the central slice from an ROI in the bottom of the left lung) is: 25.8, 22.4, 40.0, 39.2, from top to bottom (Subjects 3, 4, 8, 10). Qualitatively, ventilation abnormalities varied in size and number (arrows, Figure 2). It was found that at least one defect appeared in each set of images, including subject 9, who was on room air at the time of MRI (see Table 2). A visual comparison of approximately slice-matched ^{129}Xe ventilation images with ^1H UTE structural images showed that most (69%) ventilation abnormalities appeared to be associated with underlying structural abnormalities (Table 2). Figure 3 shows several examples of slice-matched ventilation and structural images, with apparent correspondence/non-correspondence indicated by blue and green arrows, respectively.

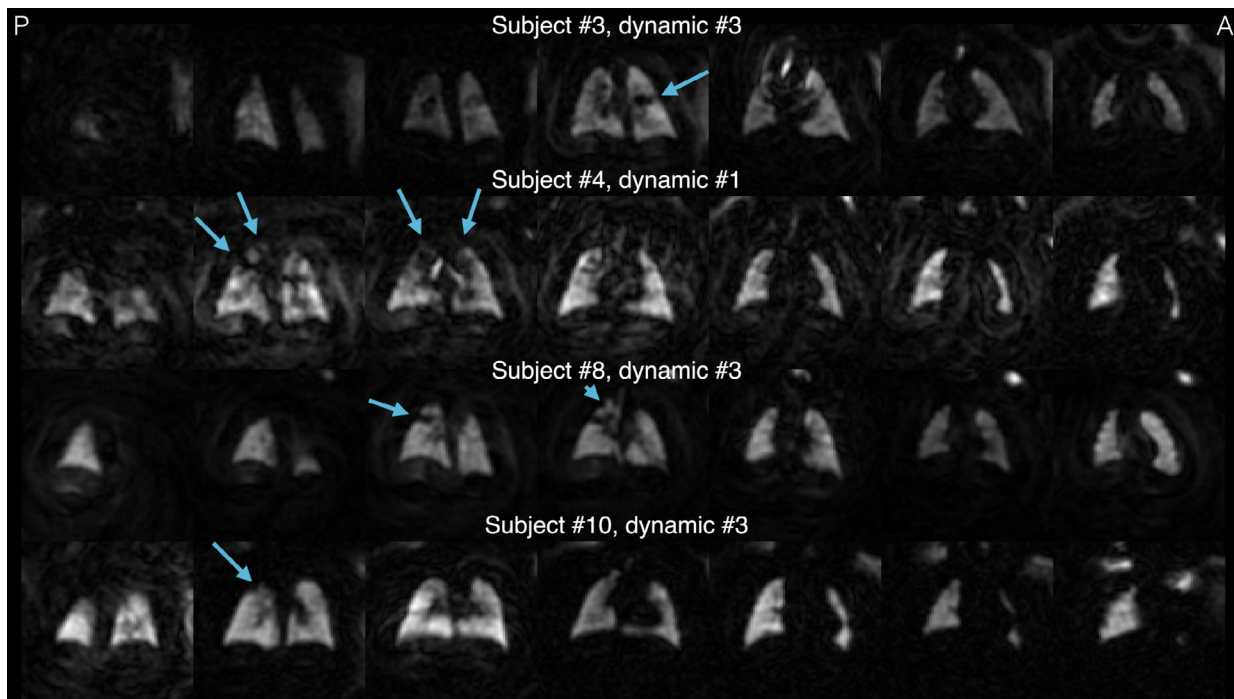


FIGURE 2 Examples of coronal ^{129}Xe spiral ventilation images (single series selected from several dynamic acquisitions) from four subjects. Qualitatively, a range of ventilation defects (regions of no/reduced signal within the lung cavity) can be observed; varying in both number and size (examples indicated by blue arrows). Subject numbers are shown (refer to Table 1). A, anterior; P, posterior.



FIGURE 3 Example comparisons of approximately slice-matched coronal images from ^{129}Xe spiral ventilation and ^1H structural UTE MRI acquisitions. In most subjects, large ventilation defects were found to correspond to structural abnormalities (blue arrows), whereas occasionally, ventilation defects did not appear to be associated with structural abnormalities (green arrow; see also Table 2). The structural defects in subjects 4 and 8 are thought to be due to atelectasis, likely related to inflammation. Anecdotally, these subjects had a total Ochiai score of 6 and 3, respectively. Subject numbers are shown (refer to Table 1).

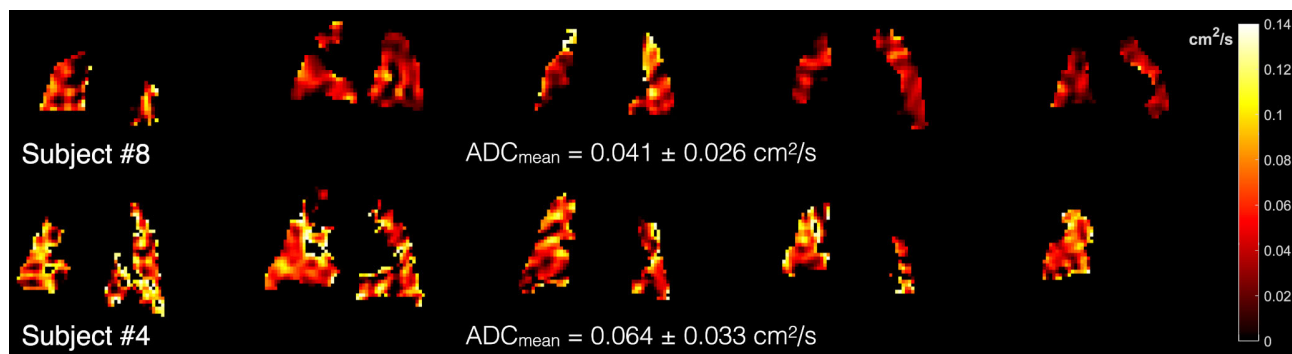


FIGURE 4 Example ^{129}Xe diffusion-weighted imaging data; apparent diffusion coefficient (ADC) maps acquired in subjects 8 and 4. Note the elevated ADC for subject 4 who was born extremely preterm (22 wk GA at birth); see also, Tables 1 and 2.

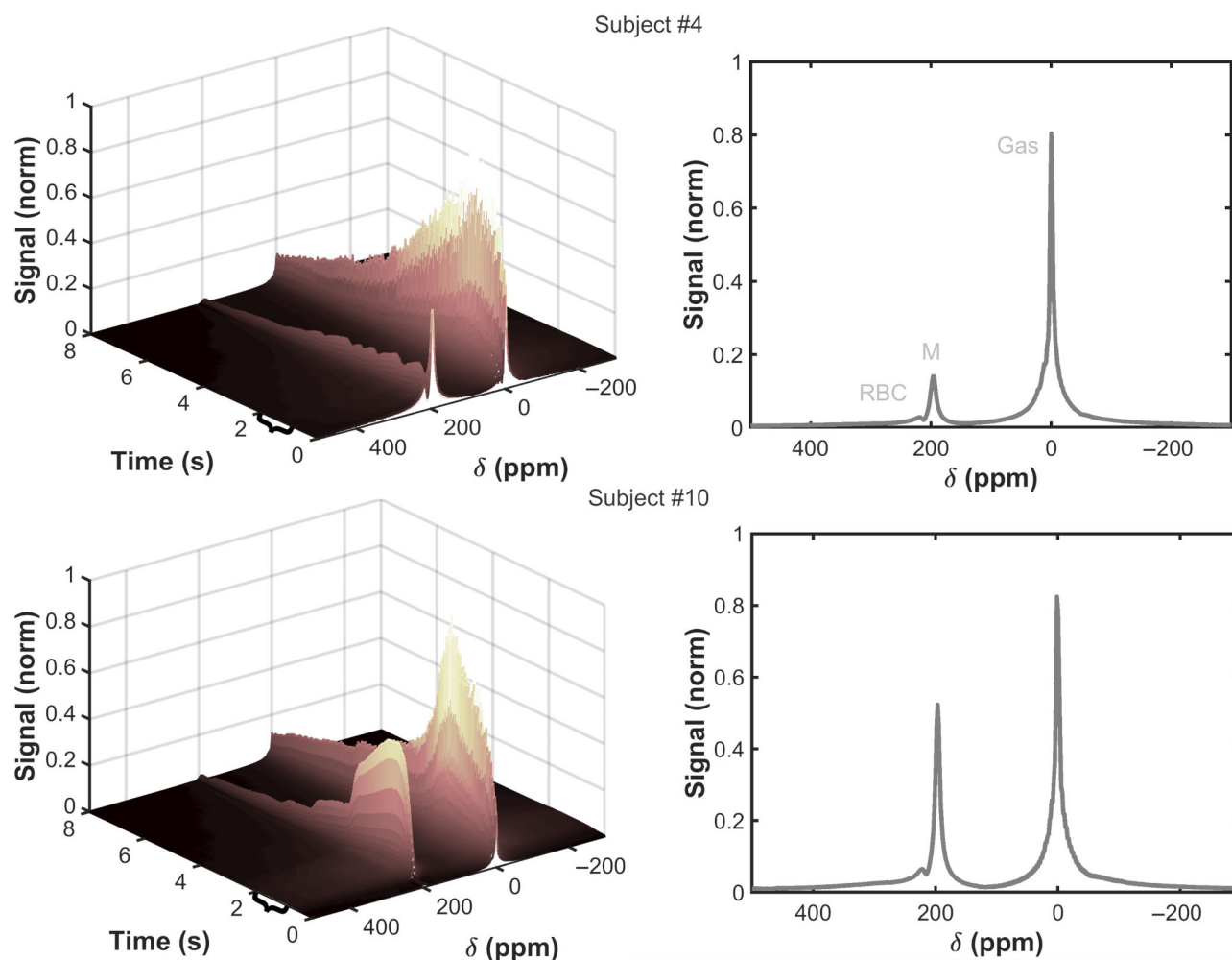


FIGURE 5 Example ^{129}Xe dynamic spectroscopy data, depicting the time series of signal intensity (left) and the mean spectra (right) obtained from averaging the spectra acquired between 1 and 2 s (region indicated by curly braces in the left plot) for two subjects. Red blood cell (RBC), tissue “membrane” (M), and gaseous ^{129}Xe resonances are indicated. Subject numbers are shown (refer to Table 1).

Mean ADC values are quoted in Table 2 and example ADC maps from two subjects are shown in Figure 4. Three of four patients had a similar ADC ($\sim 0.04 \text{ cm}^2\text{s}^{-1}$), whereas patient 4—the most pre-term subject—exhibited a significantly higher ADC of $0.064 \text{ cm}^2\text{s}^{-1}$.

^{129}Xe spectroscopy revealed a tissue membrane (M) resonance and a relatively weak red blood cell (RBC) resonance, attributed with reference to previous observations in pediatric and adult populations (Figure 5). These peaks persisted throughout the breath-hold duration, and then

the signal faded (Figure 5, left). Example mean spectra are shown in Figure 5 (right), and RBC/M ratios are listed in Table 2. The RBC resonance in the data from two patients (#3 and #6) was too low to perform accurate Lorentzian fitting, so RBC/M was assigned 0. The median (range) of RBC/M was 0.08 (0, 0.21) including all data, or 0.14 (0.06, 0.21) if the two 0 points are discounted.

4 | DISCUSSION

This work represents the first study to demonstrate the safety and feasibility of inhaled HP ^{129}Xe MRI in neonates. Although the mild O_2 desaturation associated with the Xe dose was observed almost immediately after administration (rather than the typical few seconds afterward seen in older populations), the mean decrease in SpO_2 of $-4.5 \pm 4.8\%$ is similar to that observed in a previous safety study in healthy children and participants with cystic fibrosis (mean decrease of $-6.0 \pm 7.2\%$),³⁸ and participants recovered quickly (within 10–20 s) after the initial desaturation. The images obtained here are of comparable quality to preliminary images obtained with ^3He gas in children with a range of pulmonary diseases and ages between a few months and a few years old,¹⁸ albeit with qualitatively lower SNR, which was anticipated due to the difference in gyromagnetic ratio between ^3He and ^{129}Xe . Although interpretation of the clinical significance of our findings is limited by the small number of patients and lack of a gold-standard or healthy control, it is encouraging that this method shows sensitivity to minor ventilation abnormalities in this population with mild to moderate pulmonary symptoms (and relatively low respiratory support). Although most ventilation defects appear to correspond to underlying structural abnormalities (Table 2), there is also preliminary evidence of ventilation abnormalities that appear inexplicable by lung structural changes alone, similar to those observed in children and adults with airway obstruction (see e.g., References 39,40). We anticipate that the proportion of ventilation defects that correspond to underlying structural changes would increase with disease severity; this will be evaluated in the future when further data from patients with a range of disease severities is available. However, the ventilation defect count is an imperfect metric of ventilation function, and when sufficient comparative data have been obtained in healthy normal (term-born) neonates, we will use arguably less subjective, volume-based metrics such as ventilation defect percentage⁴¹ or those of ventilation heterogeneity.⁴²

Our preliminary diffusion-weighted gas phase and dissolved-phase ^{129}Xe MR data represent the first data of their kind obtained in neonates; therefore, we can only compare our data to similar data obtained in school-aged

children and adults. The ADC values of subjects 7, 8, and 9 were all similar at $\sim 0.04 \text{ cm}^2\text{s}^{-1}$, whereas subject 4—who was born most pre-term of all patients (~ 22 wk GA at birth, compared to ~ 27 wk)—had a strikingly high ADC ($0.064 \text{ cm}^2\text{s}^{-1}$). Overall, these ADC values are higher than those previously reported in healthy children aged 6–15 y ($\sim 0.03 \text{ cm}^2\text{s}^{-1}$),³⁸ and 9- to 13-y-old children who were born prematurely with ($0.030 \pm 0.004 \text{ cm}^2\text{s}^{-1}$) and without ($0.027 \pm 0.003 \text{ cm}^2\text{s}^{-1}$) BPD,¹⁷ which may be explained by the fact that the lungs in these neonates are underdeveloped and, therefore, the alveolar surface area to volume ratio is reduced.⁴³ This is consistent with alveolar simplification in BPD and represents the first quantitative, regional metric of this aspect of premature lung disease measured in neonates. Although we are unable to report healthy comparative data here in neonates, evidence obtained with both ^3He and ^{129}Xe diffusion-weighted MRI in school-aged children shows a consistent picture of increased ADC in those who had BPD compared with those who did not.^{16,17}

Also, anecdotally we note that the (^3He) ADC values obtained from lungs with a filamin-A gene mutation are drastically higher than those obtained from healthy infant lungs ex-vivo²⁷; this mutation causes similar changes to lung structure–function to BPD.

The observation of a low RBC/M (~ 0.14) relative to school-aged children and adults (e.g., 0.31 and 0.46, respectively⁴⁴) is unexpected. The mechanism behind this observation is unclear; in future work, we plan to investigate whether fetal hemoglobin may play a role in the spectral profile of the RBC resonance. The time-course of the fetal-to-adult hemoglobin transition⁴⁵ in preterm neonates compared to term-born controls is of clinical interest. However, the interpretation of these results is limited by the effect of temporally-varying gas signals during the period of acquisition of the mean spectra; it is well known that RBC/M and similar metrics are strongly influenced by lung inflation level.⁴⁶

4.1 | Limitations

We encountered several challenges that are worthy of consideration in future neonatal ^{129}Xe MRI study design. These are summarized in Figure S2. In a few cases, inconsistency in the spiral ventilation image signal across slices was observed. This may be attributed to (i) possible errors in FA calibration resulting in the FA being set higher than the optimal value, and (ii) the interleaved acquisition order of slices (even slice numbers sequentially followed by odd slice numbers, i.e., 2,4,6,1,3,5,7, for a seven-slice scan) that could cause high signal in one slice followed by low signal in a consecutive slice due to inter-slice

gas diffusion in between slice acquisitions. Second, sequentially phase-encoded Cartesian spoiled gradient echo sequences appear unsuitable for imaging this population where the effects of imperfect gas delivery and breath-hold apnea will be accentuated in the images. As a result, signal appeared only in some of the slices of the Cartesian acquisitions. The need for high SNR and efficient k-space encoding sequences (e.g., spiral), wherein the center of k-space is sampled repeatedly, is reinforced by these observations.

Effective gas delivery is a major determinant of image quality. Whereas we have demonstrated that a short breath-hold apnea procedure is feasible in infants, manually maintaining the desired pressure through the face-mask was challenging and a major source of variability in gas delivery, and at times the resultant images indicated gas not reaching the lungs as expected. Also, the observation of SNR values that do not decrease over the first three dynamic image series (e.g., in Figure S1) is inconsistent with typical RF-induced depolarization of hyperpolarized species and implies imperfect breathhold leading to fresh gas entering the lungs during subsequent acquisitions. Furthermore, in some images, gas appears to have escaped/leaked away from the patient indicating a poor seal at the neonatal mask. This appears as signal toward the edges of the field of view. Although this can be largely removed by cropping the images and using the ^1H anatomical images as a guide, in future acquisitions, we aim to optimize the gas delivery procedure—for example using a free-breathing/multiple-breath approach with HP ^{129}Xe and O_2 gas mixtures. Such a system would need to take inspiration from automated gas-delivery systems demonstrated in both adult and small animal imaging MRI fields, as infant lung volumes lie in between these two extremes,^{47–50} and are not dissimilar from typical dead-space volumes in gas-delivery equipment. Furthermore, we will consider using an RF coil with a smaller/more lung-localized sensitive volume. In extreme cases of poor gas delivery, the gas may reach the lungs later than anticipated and therefore not be appropriately imaged (see spectroscopy acquisition in Figure S2C where instability in the gas signal and a late presentation of the dissolved-phase ^{129}Xe signal is observed). Such difficulties can complicate quantification of dissolved-phase and gaseous-phase ^{129}Xe resonances, and furthermore constrain the accuracy of FA calibration using a short TR, constant FA pulse-acquire acquisition (Figure S2D).

An additional challenge of gas delivery is in controlling the phase of the subject's respiratory cycle at which the gas is delivered. Typically, we would start from functional residual capacity in older, compliant subjects, but this is unknown in the present study. Similarly we cannot easily measure precise delivered gas volumes. Video S1

shows how 2D radial projection dynamic ^{129}Xe ventilation imaging can be used to image with high temporal resolution (0.22 s) to monitor the gas inflow and outflow, and visualize tidal breathing, which may inform the optimization of both gas delivery and acquisition methods in the future.

A further limitation is the relatively modest spatial resolution ($3 \times 3 \times 7.5 \text{ mm}^3$) of the acquired ^{129}Xe ventilation images. Whereas the slice thickness used here is half that recommended in adults,⁵¹ the in-plane resolution is only slightly higher, rather than being scaled proportionately according to lung size. This resolution is similar to that used by Altes et al. in infants and small children with ^3He gas,¹⁸ and is a compromise to minimize TR and in-turn, minimize motion artifacts. We note that the ^{129}Xe protocol (including diffusion-weighted imaging) is implemented with modest gradients (max strength 33 mT/m, max slew rate 120 T/m/s) that is, these imaging parameters should be readily achievable on other scanners. Nevertheless, the MRI set-up used here is unique—the authors are not aware of any other multi-nuclear capable NICU-housed MRI scanners at this time—and therefore replication of these results on conventional MRI scanners is needed to aid clinical adoption in this sensitive population.

In this feasibility study, only a relatively small number of patients were included, and imaging of comparatively healthy normal term-born neonates was not feasible within the scope of this work, both of which severely limit the clinical interpretation, and the extent to which we can perform reliable statistical analyses to support our results. Additionally, while all subjects were clinically diagnosed with BPD, their respiratory support requirements and disease grading aligned with more mild to moderate presentations of prematurity-related lung disease (mostly Jensen grades 1–2¹⁹). Future studies that include patients with more significant lung disease (e.g., those requiring invasive ventilation) would support the physiological interpretation of our findings.

4.2 | Conclusions

Inhaled ^{129}Xe MRI is feasible and safe in neonates with lung disease using a short breath-hold apnea technique on a dedicated multi-nuclear neonatal MRI scanner. Initial observations indicate multiple minor ventilation abnormalities, simplified/underdeveloped alveolar airspaces in extreme prematurity as measured by elevated ADC, and different dissolved-phase ^{129}Xe resonance structures compared with children and adults that are not yet understood. With further data in neonates with a broader range of BPD severity and with other pulmonary conditions of infancy, we may anticipate a future impact on infant lung disease

assessment, pending the translation of these methods to conventional MRI scanners.

ACKNOWLEDGMENTS

We acknowledge funding from National Institutes of Health R01 HL146689, Cincinnati Children's Research Foundation, European Respiratory Society (ERS) fellowship (RESPIRE3), European Commission Horizon 2020 grant agreement ID: 713406, Thrasher Research Fund Early Career Award, and the Parker B. Francis Fellowship. We also thank Prof Bastiaan Driehuis for the provision of a multi-nuclear RF amplifier, and the patients and families for their participation in this research study.

CONFLICT OF INTEREST STATEMENT

Rolf F. Schulte is an employee of GE Healthcare.

ORCID

Neil J. Stewart  <https://orcid.org/0000-0001-8358-394X>

Nara S. Higano  <https://orcid.org/0000-0002-6233-161X>

Matthew M. Willmerring  <https://orcid.org/0000-0002-4356-9622>

Jim M. Wild  <https://orcid.org/0000-0002-7246-8660>

Jason C. Woods  <https://orcid.org/0000-0002-8080-7511>

REFERENCES

- Thébaud B, Goss KN, Laughon M, et al. Bronchopulmonary dysplasia. *Nat Rev Dis Primers*. 2019;5:1-23.
- Northway WH, Moss RB, Carlisle KB, et al. Late pulmonary sequelae of bronchopulmonary dysplasia. *N Engl J Med*. 1990;323:1793-1799.
- Filippone M, Sartor M, Zacchello F, Baraldi E. Flow limitation in infants with bronchopulmonary dysplasia and respiratory function at school age. *Lancet*. 2003;361:753-754.
- Lesnick BL, Davis SD. Infant pulmonary function testing: overview of technology and practical considerations—new current procedural terminology codes effective 2010. *Chest*. 2011;139:1197-1202.
- Miglioretti DL, Johnson E, Williams A, et al. The use of computed tomography in pediatrics and the associated radiation exposure and estimated cancer risk. *JAMA Pediatr*. 2013;167:700-707.
- Higano NS, Hahn AD, Tkach JA, et al. Retrospective respiratory self-gating and removal of bulk motion in pulmonary UTE MRI of neonates and adults. *Magn Reson Med*. 2017;77:1284-1295.
- Higano NS, Fleck RJ, Spielberg DR, et al. Quantification of neonatal lung parenchymal density via ultrashort echo time MRI with comparison to CT. *J Magn Reson Imaging*. 2017;46:992-1000.
- Higano NS, Spielberg DR, Fleck RJ, et al. Neonatal pulmonary MRI of bronchopulmonary dysplasia predicts short-term clinical outcomes. *Am J Respir Crit Care Med*. 2018;198:1302-1311.
- Zanette B, Schrauben EM, Munidasa S, et al. Clinical feasibility of structural and functional MRI in free-breathing neonates and infants. *J Magn Reson Imaging*. 2022;55:1696-1707.
- Dyke JP, Voskrebenezov A, Blatt LK, et al. Assessment of lung ventilation and perfusion of premature infants with bronchopulmonary dysplasia at 1.5 tesla using phase-resolved functional lung (PREFUL) magnetic resonance imaging (MRI) in the NICU. *Pediatr Radiol*. 2023;53:1076-1084. 10.1007/s00247-023-05598-6
- Stewart NJ, Smith LJ, Chan H-F, et al. Lung MRI with hyperpolarised gases: current & future clinical perspectives. *BJR*. 2022;95:20210207.
- Thomen RP, Walkup LL, Roach DJ, Cleveland ZI, Clancy JP, Woods JC. Hyperpolarized ^{129}Xe for investigation of mild cystic fibrosis lung disease in pediatric patients. *J Cyst Fibros*. 2017;16:275-282.
- Driehuis B, Martinez-Jimenez S, Cleveland ZI, et al. Chronic obstructive pulmonary disease: safety and tolerability of hyperpolarized ^{129}Xe MR imaging in healthy volunteers and patients. *Radiology*. 2012;262:279-289.
- Wang JM, Robertson SH, Wang Z, et al. Using hyperpolarized ^{129}Xe MRI to quantify regional gas transfer in idiopathic pulmonary fibrosis. *Thorax*. 2018;73:21-28.
- Altes TA, Mata J, Froh DK, Paget-Brown A, de Lange EE, Mugler JP. Abnormalities of Lung Structure in Children with Bronchopulmonary Dysplasia as Assessed by Diffusion Hyperpolarized Helium-3 MRI. International Society for Magnetic Resonance in Medicine Annual Meeting, Seattle. 2006 #86.
- Flors L, Mugler JP, Paget-Brown A, et al. Hyperpolarized Helium-3 diffusion-weighted magnetic resonance imaging detects abnormalities of lung structure in children with bronchopulmonary dysplasia. *J Thorac Imaging*. 2017;32:323-332.
- Chan H-F, Smith LJ, Biancardi AM, et al. Image phenotyping of preterm-born children using hyperpolarised ^{129}Xe lung MRI and multiple-breath washout. *Am J Respir Crit Care Med*. 2023;207:89-100.
- Altes TA, Meyer CH, Mata JF, et al. Hyperpolarized helium-3 magnetic resonance lung imaging of non-sedated infants and young children: a proof-of-concept study. *Clin Imaging*. 2017;45:105-110.
- Jensen EA, Dysart K, Gantz MG, et al. The diagnosis of bronchopulmonary dysplasia in very preterm infants. An evidence-based approach. *Am J Respir Crit Care Med*. 2019;200:751-759.
- Tkach JA, Hillman NH, Jobe AH, et al. An MRI system for imaging neonates in the NICU: initial feasibility study. *Pediatr Radiol*. 2012;42:1347-1356.
- Tkach JA, Merhar SL, Kline-Fath BM, et al. MRI in the neonatal ICU: initial experience using a small-footprint 1.5-T system. *Am J Roentgenol*. 2014;202:W95-W105.
- Pratt R, Giaquinto R, Loew W, et al. A $^{129}\text{Xe}/^1\text{H}$ switched frequency high pass birdcage coil for hyperpolarized ^{129}Xe gas lung imaging in neonates at 1.5 T. *Int Soc Mag Reson Med*. 2021;3563.
- Pratt R, Giaquinto R, Ireland C, et al. A novel switched frequency $^3\text{He}/^1\text{H}$ high-pass birdcage coil for imaging at 1.5 tesla. *Concepts Mag Reson Part B Magn Reson Eng*. 2015;45:174-182.
- Salerno M, Altes TA, Brookeman JR, De Lange EE, Mugler JP. Rapid hyperpolarized ^3He diffusion MRI of healthy and emphysematous human lungs using an optimized interleaved-spiral pulse sequence. *J Magn Reson Imaging*. 2003;17:581-588.

25. Sukstanskii AL, Yablonskiy DA. Lung morphometry with hyperpolarized ^{129}Xe : theoretical background. *Magn Reson Med*. 2012;67:856-866.
26. Chan H-F, Stewart NJ, Norquay G, Collier GJ, Wild JM. 3D diffusion-weighted ^{129}Xe MRI for whole lung morphometry. *Magn Reson Med*. 2018;79:2986-2995.
27. Higano NS, Thomen RP, Quirk JD, et al. Alveolar airspace size in healthy and diseased infant lungs measured via hyperpolarized ^3He gas diffusion magnetic resonance imaging. *Neonatology*. 2020;117:704-712.
28. Bier EA, Robertson SH, Schrank GM, et al. A protocol for quantifying cardiogenic oscillations in dynamic ^{129}Xe gas exchange spectroscopy: the effects of idiopathic pulmonary fibrosis. *NMR Biomed*. 2019;32:e4029.
29. Yip C, Fessler JA, Noll DC. Iterative RF pulse design for multidimensional, small-tip-angle selective excitation. *Magn Reson Med*. 2005;54:908-917.
30. Wild JM, Paley MNJ, Kasuboski L, et al. Dynamic radial projection MRI of inhaled hyperpolarized ^3He gas. *Magn Reson Med*. 2003;49:991-997.
31. Marshall H, Xu X, Norquay G, Parnell SR, Parra-Robles J, Wild JM. Dynamic radial imaging of inhaled ^{129}Xe and ^3He . *Proc Intl Soc Mag Reson Med*. 20. Melbourne, VIC, Australia; 2012:4000.
32. Hahn AD, Higano NS, Walkup LL, et al. Pulmonary MRI of neonates in the intensive care unit using 3D ultrashort echo time and a small footprint MRI system. *J Magn Reson Imaging*. 2017;45:463-471.
33. Beatty PJ, Nishimura DG, Pauly JM. Rapid gridding reconstruction with a minimal oversampling ratio. *IEEE Trans Med Imaging*. 2005;24:799-808.
34. Brender JR, Kishimoto S, Merkle H, et al. Dynamic imaging of glucose and lactate metabolism by ^{13}C -MRS without hyperpolarization. *Sci Rep*. 2019;9:3410.
35. Chang YV, Quirk JD, Russet IC, Atkinson JJ, Hersman FW, Woods JC. Quantification of human lung structure and physiology using hyperpolarized ^{129}Xe . *Magn Reson Med*. 2014;71:339-344.
36. Wang Z, Bier EA, Swaminathan A, et al. Diverse cardiopulmonary diseases are associated with distinct xenon MRI signatures. *Eur Respir J*. 2019;54:1900831.
37. Hillman BA, Tabrizi MN, Gauda EB, Carson KA, Aucott SW. The neonatal pain, agitation and sedation scale and the bedside nurse's assessment of neonates. *J Perinatol*. 2015;35:128-131.
38. Walkup LL, Thomen RP, Akinyi TG, et al. Feasibility, tolerability and safety of pediatric hyperpolarized ^{129}Xe magnetic resonance imaging in healthy volunteers and children with cystic fibrosis. *Pediatr Radiol*. 2016;46:1651-1662.
39. Thomen RP, Walkup LL, Roach DJ, et al. Regional structure-function in cystic fibrosis lung disease using hyperpolarized ^{129}Xe and ultrashort echo magnetic resonance imaging. *Am J Respir Crit Care Med*. 2020;202:290-292.
40. Marshall H, Horsley A, Taylor CJ, et al. Detection of early subclinical lung disease in children with cystic fibrosis by lung ventilation imaging with hyperpolarised gas MRI. *Thorax*. 2017;72:760-762.
41. Eddy RL, Svenningsen S, McCormack DG, Parraga G. What is the minimal clinically important difference for helium-3 magnetic resonance imaging ventilation defects? *Eur Respir J*. 2018;51:1800324.
42. Tzeng Y-S, Lutchen K, Albert M. The difference in ventilation heterogeneity between asthmatic and healthy subjects quantified using hyperpolarized ^3He MRI. *J Appl Physiol*. 2009;106:813-822.
43. Coalson JJ. Pathology of new bronchopulmonary dysplasia. *Semin Neonatol*. 2003;8:73-81.
44. Willmering MM, Walkup LL, Niedbalski PJ, et al. Pediatric ^{129}Xe gas-transfer MRI—feasibility and applicability. *J Magn Reson Imaging*. 2022;56:1207-1219.
45. Sankaran VG, Orkin SH. The switch from fetal to adult hemoglobin. *Cold Spring Harb Perspect Med*. 2013;3:a011643.
46. Hahn AD, Kammerman J, Evans M, et al. Repeatability of regional pulmonary functional metrics of hyperpolarized ^{129}Xe dissolved-phase MRI. *J Magn Reson Imaging*. 2019;50:1182-1190.
47. Obert AJ, Kern AL, Gutberlet M, et al. Volume-controlled 19F MR ventilation imaging of fluorinated gas. *J Magn Reson Imaging*. 2023;57:1114-1128.
48. Halaweish AF, Charles HC. Physiorack: an integrated MRI safe/conditional, gas delivery, respiratory gating, and subject monitoring solution for structural and functional assessments of pulmonary function. *J Magn Reson Imaging*. 2014;39:735-741.
49. Imai H, Kimura A, Hori Y, et al. Hyperpolarized ^{129}Xe lung MRI in spontaneously breathing mice with respiratory gated fast imaging and its application to pulmonary functional imaging. *NMR Biomed*. 2011;24:1343-1352.
50. Virgincar RS, Dahlke J, Robertson SH, et al. A portable ventilator with integrated physiologic monitoring for hyperpolarized ^{129}Xe MRI in rodents. *J Magn Reson*. 2018;295:63-71.
51. Niedbalski PJ, Hall CS, Castro M, et al. Protocols for multi-site trials using hyperpolarized ^{129}Xe MRI for imaging of ventilation, alveolar-airspace size, and gas exchange: a position paper from the ^{129}Xe MRI clinical trials consortium. *Magn Reson Med*. 2021;86:2966-2986.

SUPPORTING INFORMATION

Additional supporting information may be found in the online version of the article at the publisher's website.

Figure S1. Example series of dynamic coronal ^{129}Xe spiral ventilation images acquired in Subject #3. Five out of ten total acquired dynamic image series are shown, and the average images (generated via averaging of each spiral arm prior to gridding) from these five dynamic image series are shown in the purple box. In most cases, the strongest signals were observed in the first three dynamic series of images (i.e., during the supposed breath-hold period), with some signal maintained for dynamics four and five, but tending to tail off in subsequent acquisitions. For this example, the SNR was as follows for the five dynamic image series shown, respectively: 27.2, 26.3, 25.8, 25.0, 7.7.

Figure S2. Illustrative examples of some of the challenges encountered with gas delivery to infants via breath-hold. (A) Spiral acquisition wherein consecutive slices appear to

have signal discontinuities, assumed to be due to an inappropriately high flip angle. (B) Single Cartesian acquisition image series, wherein signal was found to appear in only one slice. This again indicates signal instability, and the unsuitability of sequentially encoded acquisitions (i.e., the need to sample the center of k-space more frequently). (C) Spectroscopic acquisition where the gas resonance shows two waves of signal, indicating imperfect gas delivery. It can be seen in the dissolved-phase resonance(s) that a bolus of gas arrived to the lungs late (again, note that spectra from the region indicated by the curly braces are those used to calculate the mean spectrum). (D) Example of a flip angle calibration scan where the signal decay was unstable due to fluctuating gas delivery, and thus the accuracy of the fit for flip angle is constrained. Subject numbers are shown (refer to Table 1).

Table S1. Change in Blood Oxygen Saturation (SpO₂) during Xe inhalation.

Video S1. 2D radial projection dynamic ¹²⁹Xe ventilation imaging in Subject #10, using a sliding window (50% view sharing) method to reconstruct images with a temporal resolution of 0.22 s. This indicates that ¹²⁹Xe gas is already saturating the lungs at the beginning of the acquisition, and stays in the lungs for several seconds during normal breathing (as can be seen by diaphragmatic movement on the images). Exhalation of gas through the central airway can be observed. The video stops after the gas has washed out of the lungs.

How to cite this article: Stewart NJ, Higano NS, Mukthapuram S, et al. Initial feasibility and challenges of hyperpolarized ¹²⁹Xe MRI in neonates with bronchopulmonary dysplasia. *Magn Reson Med.* 2023;1-12. doi: 10.1002/mrm.29808